RSC Advances

PAPER

View Article Online
View Journal | View Issue

Cite this: *RSC Adv.*, 2026, **16**, 22204

Synthesis and surface functionalization of gold microtubes for SERS detection of dyes

Ainur B. Khairusheva [ab] and Ilya V. Korolkov*[ab]

In this study, we report on the synthesis of gold microtube-based substrates and their organic modification with 11-mercaptoundecanoic acid (MUA11) for the use in surface-enhanced Raman spectroscopy (SERS). The main objective of the work was to investigate the influence of organic modification on the optical properties of the substrates and the degree of Raman signal enhancement. The synthesis of gold microtubes was carried out using a chemical template-assisted growth method, resulting in the formation of uniform and continuous gold layers on the porous template surface. The obtained structures were characterized by X-ray diffraction (XRD), scanning electron microscopy with energy-dispersive X-ray analysis (SEM-EDX). Localized surface plasmon resonance (LSPR) behavior was analyzed through the optical response of the gold microtubes. The presence and efficiency of the organic modification were verified by X-ray photoelectron spectroscopy (XPS). Optical characterization revealed that the substrates with uniformly distributed gold microtubes exhibited a plasmonic resonance around 440–470 nm. To evaluate the analytical performance of the developed substrates, SERS analyses were performed using three model organic dyes: methylene blue, methyl violet, methyl red, in a concentration range from 10^{-2} to 10^{-6} M.

Received 11th February 2026
Accepted 15th April 2026

DOI: 10.1039/d6ra01224h

rsc.li/rsc-advances

1 Introduction

Surface-enhanced Raman Scattering (SERS) has become an indispensable analytical technique for the detection and characterization of hazardous compounds due to its non-destructive nature, rapid acquisition, high sensitivity, and ability to provide unique vibrational fingerprints of molecules.[1,2] The enhancement of Raman scattering in SERS arises from two fundamental mechanisms. The electromagnetic mechanism (EM) is associated with the excitation of localized surface plasmons and resulting amplification of the electromagnetic field near metallic nanostructure.[3,4] The chemical mechanism (CM), in contrast, originates from charge–transfer interactions between the analyte and the metal surface, which contribute to additional signal amplification and molecular selectivity. Together, these mechanisms allow SERS to achieve several orders of magnitude signal enhancement, making it suitable for trace detection across diverse application fields.[5,6]

Traditional methods for detecting such compounds, including UV-Vis spectroscopy, FTIR, HPLC, and mass spectrometry, are reliable but often laborious, destructive, or require relatively high analyte concentrations. By contrast, SERS offers rapid, non-destructive detection at trace levels, providing molecular specificity with minimal sample volumes.

Organic dyes are among the most common water pollutants due to their widespread industrial use and high stability. In addition to dyes, other hazardous organic compounds such as pesticides also pose serious environmental and health risks. Therefore, the development of sensitive and selective detection methods for a broad range of pollutants remains a critical challenge. In this context, SERS-based platforms offer significant potential.[7–9]

In summary, the progress of nanoscale materials science has been instrumental in advancing SERS-based detection technologies.[10] The rational design of SERS-active substrates requires careful control over both physical parameters such as morphology, size, dispersion and chemical factors, including functionalization and selective molecular interactions. Achieving a balance between uniformity, stability, and activity remains one of the central challenges in the field. The integration of structural engineering with targeted surface chemistry provides a promising pathway toward the development of the highly sensitive, selective, and reliable SERS platforms for applications in environmental monitoring,[11] food safety,[12] medicine, and other areas of high societal relevance.[9,13]

The efficiency of SERS is strongly dependent on the properties of the substrates employed. Material composition, morphology, and dimensional characteristics determine the distribution of local electromagnetic fields and thus the degree of signal amplification.[14] Over the past decades, a variety of

[a]*The Institute of Nuclear Physics ARKAE, 050032, Ibragimov str., 1, Almaty, Kazakhstan. E-mail: i.korolkov@inp.kz*

[b]*L.N. Gumilyov Eurasian National University, Satbaev str. 5, 010008, Astana, Kazakhstan*

substrates have been developed, with metal colloidal systems, flexible supports, and solid-state platforms emerging as the most prominent. Metal colloids, typically synthesized *via* chemical reduction of noble metals such as Au, Ag,[15] Ni,[16] or Cu, are particularly attractive due to the relative simplicity, reproducibility, and scalability of this method.[7,17,18] The size and morphology of the nanoparticles can be finely tuned by adjusting precursor concentration, reducing agents, or reaction conditions, thereby allowing control over plasmonic properties.[19] Flexible substrates, often prepared by depositing nanoparticles onto paper, polymer films, or adhesive supports, offer mechanical adaptability and cost-effectiveness, while solid-state platforms provide robust and reusable SERS- active surfaces, ensuring stability and reproducibility of measurements.[20,21]

Advances in nanotechnology have also enabled the development of multifunctional and hybrid nanostructures that further enhance SERS activity. For instance, magnetic nanoparticles coated with noble metals can significantly improve signal intensity when subjected to an external magnetic field, due to the intensified local electromagnetic field around the nanostructures. In parallel, bifunctional organic molecules such as 11-mercaptoundecanoic acid (MUA), cysteine, and glutathione are frequently employed to induce controlled self-assembly of nanoparticles.[22] These molecules establish interparticle connections through hydrogen bonding or electrostatic interactions, promoting aggregation at the nanoscale. The resulting nanoparticle clusters produce shifts in localized surface plasmon resonance (LSPR) and nanoscale junctions known as "hot spots", which serve as principal sites of Raman enhancement.[20,23,24]

The presence of hot spots is widely recognized as the decisive factor in achieving ultrasensitive detection. Localized electromagnetic fields at sharp edges or interparticle junctions can enhance the Raman signal by several orders of magnitude, enabling the identification of analytes at extremely low concentrations.[25,26] However, the effectiveness of hot spots strongly depends on the spatial distribution and dispersion of nanostructures.[27] Well-dispersed nanoparticles or microtubes generate localized regions of enhancement, whereas dense, uncontrolled agglomerates may induce strong background fluorescence and compromise spectral quality. To address these challenges, chemical surface modification is employed to improve molecular adsorption and selectivity. Functionalization with molecules such as 11-mercaptoundecanoic acid provides active binding sites for dyes, pesticides, and other hazardous compounds, thereby combining enhanced sensitivity with chemical specificity.[28–30]

In SERS-based detection, the adsorption behavior of analytes on metallic substrates plays a decisive role in determining both the intensity and the reproducibility of the Raman signal.[31] Organic dyes such as methylene blue (MB), methyl red (MR), and methyl violet (MV) are frequently employed as model analytes due to their well-defined molecular structures and strong affinity for metallic surfaces. MB is a cationic thiazine dye of which positively charged heterocyclic ring system.[32,33] MR, in contrast, is an azo dye that exists in zwitterionic or anionic forms depending on the solution pH. MV is cationic triphenylmethane dye, however, its bulky molecular structure may restrict orientation on the surface, thereby influencing the relative intensities of its Raman bands. The presence of MUA11 functionalization introduces terminal carboxylate groups that alter the electrostatic environment of the substrate, can enhance the binding of cationic dyes such as MB and MV ultimately improving both selectivity and reproducibility of SERS signals.

In this article, gold-coated substrates before and after modification with COOH groups were investigated. The effect of modification on signal intensity and selectivity at low analyte concentrations was examined. The obtained results demonstrate that the molecular structure of each dye influences the adsorption behavior and interaction with the modified gold surface in district manner.[1,33] Thus, the aim of the surface functionalization with MUA is to tailor the surface chemistry of Au microtubes and to improve the adsorption of probe molecules, thereby enhancing the SERS performance.

2 Experimental methods

2.1 Materials

Sodium sulfite (Na_2SO_3, 98%), sodium bicarbonate ($NaHCO_3$), sodium gold sulfite $Na_3[Au(SO_3)_2]$, stannous chloride dihydrate ($SnCl_2 \cdot 2H_2O$, 98%), and silver nitrate ($AgNO_3$, 98%) were purchased from Sigma-Aldrich (St. Louis, MO, USA). Aqueous ammonia (NH_4OH, 25%) was obtained from Sigma-Tek. Barium hydroxide ($Ba(OH)_2$) (analytical grade), methyl red ($C_{15}H_{15}N_3O_2$), and methyl violet ($C_{24}H_{28}N_3Cl$) were purchased from Sigma-Aldrich (St. Louis, MO, USA). Methylene blue ($C_{16}H_{18}ClN_3S$) was purchased from Sigma-Aldrich (China). All chemicals were of analytical grade and used without further purification. Mercaptoundecanoic acid 11 (MUA11) was obtained from Sigma-Aldrich (India).

2.2 Synthesis of Au microtubes

Polyethylene terephthalate (PET) track-etched membranes (thickness 12 μm) were obtained by irradiation of PET film with accelerated Kr ions and subsequent chemical etching in NaOH solution, yielding channels with diameters of 1.5 ± 0.23 μm, followed by an oxidation step performed according to the procedure described in.[34,35]

The gold plating precursor, sodium disulfitoaurate (I) ($Na_3[Au(SO_3)_2]$), was synthesized from $HAuCl_4 \cdot 3H_2O$ using aqua regia ($HNO_3 : HCl = 1 : 3$), followed by treatment with $Ba(OH)_2$ and Na_2SO_3 as described previously.[36]

Template-assisted deposition of Au microtubes was carried out in three sequential steps: sensitization with $SnCl_2$, activation with $AgNO_3$ and NH_4OH, and chemical deposition using Na_2SO_3, $NaHCO_3$, and $Na_3[Au(SO_3)_2]$, all performed in deionized water. The resulting PET membranes containing Au microtubes were characterized by gravimetric analysis (before and after deposition) and gas permeability measurements to evaluate tube formation and pore size.

The template-assisted growth of Au microtubes is based on the reduction of Au(I) complexes within the confined geometry

of track-etched channels. Sensitization with $SnCl_2$ introduces catalytic sites, which are subsequently activated by Ag^+ ions through a redox exchange, forming metallic silver nuclei. These nuclei act at catalytic centers for the reduction of Au(I) complexes in the presence of Na_2SO_3 and $NaHCO_3$. The confined deposition inside PET pores promotes the growth of hollow tubular structures rather than solid nanowires, while additional etching and oxidation steps regulate pore size and surface functionality. Building upon this synthetic approach, recent studies have emphasized the importance of post-synthetic surface modification to further enhance the performance of gold microtubes.[37]

2.3 Organic modification with 11-mercaptoundecanoic acid

The obtained gold microtubes were modified with carboxyl groups. As modifying reagent, 11-mercaptoundecanoic acid (MUA11) was used. The synthesized gold microtubes (1 mg) were immersed in a 0.5 mM MUA11 solution prepared in isopropanol (1 ml). The mixture was kept under vigorous stirring for 24 hours. Finally, the microtubes were rinsed 5–6 times with isopropanol to remove unbound molecules and residual reagents. As a result, organically modified gold microtubes were obtained.

Other concentrations of MUA11 such as 0.1, 0.25 and 1 mM were also tested, but no significant difference in elemental composition was detected.

2.4 Gas permeability measurements

Gas permeation experiments were performed by applying a controlled pressure gradient (ΔP) across the PET membrane containing gold microtubes. The effective pore sizes of the membranes were calculated from gas permeability based on Hagen–Poiseuille equation.[38]

$$r = \left(\frac{8\eta l Q}{\pi n \Delta P}\right)^{1/4} \quad (1)$$

where, r – pore radius [m], Q is liquid flux ($m^3\ cm^{-2}$), n – number of pores at the membrane surface [m^{-2}], η – gas viscosity [N s m^{-2}], ΔP – applied pressure [Pa], l -thickness of the membrane.

2.5 Structural characterization

X-ray diffraction (XRD) analysis was carried out at ambient temperature using a SmartLab diffractometer (Rigaku Corporation, Tokyo, Japan), which was equipped with a Cu-Kα radiation source ($\lambda = 1.5406$ Å), ensuring high-resolution diffraction measurements. The collected diffraction data were subsequently processed, refined, and analyzed with the aid of DIFFRAC. EVA software (version 4.2.1: Bruker AXS GmbH, Karlsruhe, Germany), which provided reliable phase identification and structural characterization.

In addition, the investigation of surface morphology together with elemental composition was performed using scanning electron microscopy (SEM) on a Phenom ProX G6 scanning electron microscope (Thermo Fisher Scientific, Eindhoven, The Netherlands), which also allowed energy-dispersive spectroscopy to be applied for qualitative and semi-quantitative elemental analysis of the samples.

The Thermo Scientific Nexsa XPS System was used to analyze the surface composition and chemical states of the samples. This method provided detailed information about the elements present and their bonding environments, allowing precise evaluation of surface modifications and material interactions.

2.6 Optical characterization

To evaluate the plasmonic properties of the synthesized Au and Au@MUA11 microtubes, UV-visible absorption spectra were recorded using an Analytik Jena Specord 250 Plus spectrophotometer equipped with an integrating sphere.

The spectra were acquired in the wavelength range of 300–1100 nm with a resolution of 1 nm and a scan rate of 10 nm s^{-1}. Barium sulfate was used as a reference standard, and baseline correction was performed before measurements.

2.7 SERS measurements

Gold microtubes and Au@MUA11 microtubes deposited on the silicon plate were used for SERS measurements. Methylene blue, methyl violet and methyl red dyes were used for testing. Raman spectra were collected using an EnSpectr microscope equipped with excitation lasers of 532 nm. The spectral range of interest was 1000–1800 cm^{-1}, which encompasses the characteristic vibrational modes of the selected dyes.

In practice, the exact determination of N_{SERS} and N_{Raman} is challenging for a complex nanostructured substrate due to the non-uniform distribution electromagnetic hotspots. Therefore, a commonly used approximation was employed, assuming that the number of molecules contributing to the Raman signal is proportional to their concentration within the laser probing volume, provided that identical experimental conditions are used for both SERS and normal Raman measurements.

The surface-enhanced Raman scattering (SERS) enhancement factor (EF) was determined according to the expression eqn (2):

$$EF = \frac{(A_{SERS}/C_{SERS})}{(A_{Raman}/C_{Raman})} \quad (2)$$

where A_{SERS} and A_{Raman} are Raman peak areas measured under SERS and conventional Raman conditions, respectively. C_{SERS} and C_{Raman} are the corresponding analyte concentrations.

Physically, this ratio quantifies the amplification of the Raman signal per molecule, arising primarily from the electromagnetic mechanism associated with LSPR excitation in metallic nanostructures. It should be noted that this method provides an approximate, order-of-magnitude estimation of the EF rather than an absolute value.

The sensitivity of the fabricated substrates was evaluated by estimating the limit of detection (LOD), calculated according to the following relation eqn (3):

$$LOD = 3 \times \left(\frac{\sigma}{s}\right) \quad (3)$$

where σ – represent the standard deviation of the blank measurement, and s – is the slope of the calibration curve. This criterion defines the lowest analyte concentration that can be reliably distinguished from the background signal. The combination of SERS enhancement and precise LOD determination allowed us to assess both the amplification efficiency of the gold microtubes and their analytical potential for trace-level detection.[39]

3 Results and discussion

3.1 Morphology and structure

Fig. 1 presents the diffraction patterns of Au and Au@MUA11 MTs structures. Both samples exhibit strong diffraction peaks at $2\theta \approx 38.2°$, 44.4°, 64.6°, 77.5°, and 82.3°, which correspond to reflection from the (111), (200), (220), (311), and (222) planes of FCC gold. The most intense reflection at (111) indicates a preferred crystallographic orientation in this direction, which is characteristic of nanostructured gold materials. The calculated lattice parameters were $a = 4.0777(6)$ Å for Au and $a = 4.0777(8)$ Å for Au@MUA11, which are in good agreement with the standard value for bulk Au ($a = 4.078$ Å JCPDS 04-0784). This confirms the formation of a well-ordered crystalline lattice without significant distortions. The average crystalline size obtained from the Scherrer equation was 15.5 ± 2.2 nm for Au and 14.6 ± 2.7 nm for Au@MUA11 (Table 1). This difference is statistically insignificant and falls within the margin of error, indicating that the surface modification with MUA11 does not affect the crystallite size. Importantly, no additional peaks corresponding to impurity phases (such as a gold oxides or residual compounds) were observed, which confirms the phase purity of the synthesized samples.

In addition to the crystallographic analysis, the sharpness and intensity of the diffraction peaks indicate a high degree of crystallinity in both Au and Au@MUA11 microtubular structures. The slight broadening of the reflections in the functionalized sample suggests a reduction in crystallite size and possible introduction of micro strain due to the organic coating, yet the overall preservation of the FCC gold phase confirms that the functionalization process does not alter the fundamental crystal structure. It should be also noted that the gold microtubes are composed of many small gold crystallites. The crystallite size obtained from XRD (~15.5 ± 2.2 nm and 14.6 ± 2.7 nm) represents these nanoscale building units, while the SEM images show the larger tubular structures formed by their assembly (Fig. 2a and b).

The microtubes exhibit a diameter of approximately 1.4 ± 0.21 μm (Table 2), while their length extends to 12 μm. Such as arrangement is dictated by the orientation of pores in the track-etched membrane, which directs the growth and results in predominantly parallel alignment of the microtubes. The tube surfaces are rough and heterogeneous, which is particularly important for the generation of "hot spots" responsible for strong SERS enhancement.[40] Fig. 2c and d also shows the elemental composition using a Scanning Electron Microscope.

The EDX spectra (Fig. 2e and f) further confirm the presents of Au, Ag, Sn and C. Pronounced peaks corresponding to gold indicate successful gold deposition. Weak silver signals may originate from residual impurities of the synthesis process or partial alloying of the surface. The high carbon content is attributed to the sample preparation procedure, as carbon adhesive tape was used to fix the sample. The presence of oxygen can be attributed to remnants of the polymer matrix (PET). A comparison of spectra before and after modification demonstrates appearance of S but with low intensity. Due to peak overlap between sulfur and gold, EDX cannot reliably confirm sulfur presence. Therefore, XPS analysis, offering higher sensitivity and chemical specificity, is used as the primary method is discussed in detail below.

The survey XPS spectra of Au MTs (Fig. 3a) reveal characteristic photo-emission peaks corresponding to Au, Ag, Sn, O, C. In addition to the same elements, S was also registered on the sample Au@MUA11 MTs (Fig. 3b) and C with much higher intensity. The high-resolution S 2p XPS spectrum of the Au@MUA11 MTs sample (Fig. 3g) was deconvoluted into two spin–orbit doublets, maintaining a fixed energy separation of 1.18 eV and an area ration of 2 : 1 between the S $2p_{3/2}$ and S $2p_{1/2}$ components. The resulting fitting model provides good agreement with the experimental data ($R^2 = 0.956$), confirming the presence of two chemically distinct sulfur species on the surface. The first doublet exhibits a major component at S $2p_{3/2}$ = 161.1 eV and S $2p_{1/2}$ = 162.3 eV, which is characteristic of metal-sulfur (Au–S) bonds. This lower binding energy region

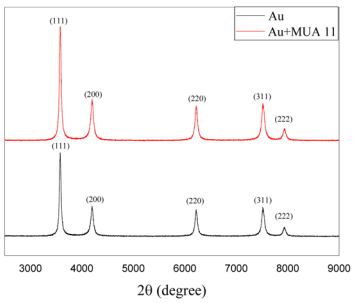

Fig. 1 XRD of Au and Au@MUA11 MTs.

Table 1 Structural parameters of Au and Au@MUA11 microtubes

No.	Phase	(*hkl*)	2θ°	*d*, Å	Crystallite size, nm	Lattice parameter, Å	Phase concentration, 100%
Au	Au – Cubic, $Fm\bar{3}m$ (111)	1 1 1	38.19702	2.35425	15.5 ± 2.2	4.07769 (6)	100%
Au@MUA 11	Au@MUA 11 – Cubic, $Fm\bar{3}m$ (111)	1 1 1	38.19673	2.35427	14.6 ± 2.7	4.07772 (8)	100%

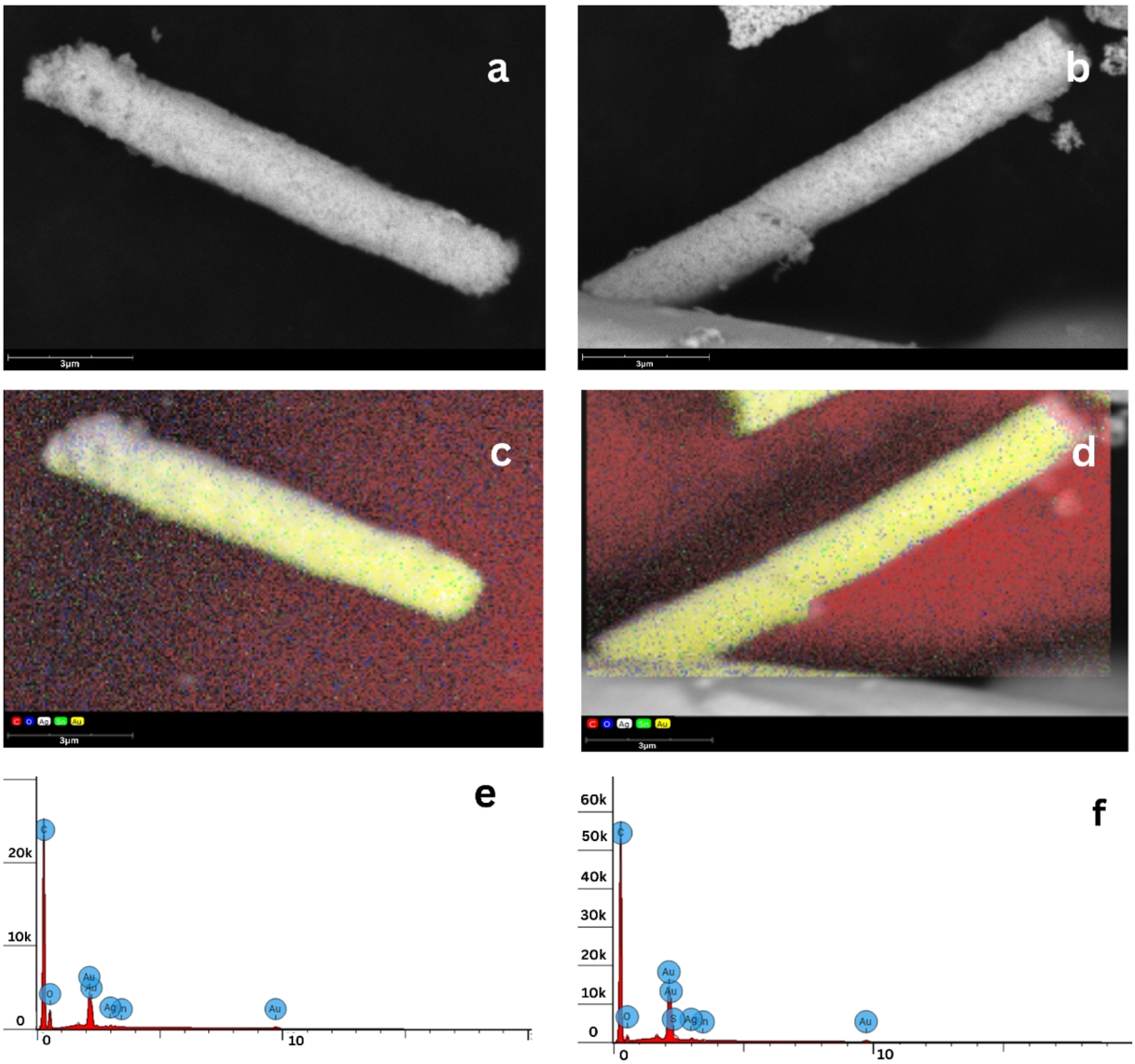

Fig. 2 SEM images, EDX mapping and corresponding EDX spectra of Au (a, c and e) and Au@MUA11 microtubes (b, d and f).

Table 2 Elemental composition from XPS survey spectra

Sample	C (at%)	O (at%)	Au (at%)	Ag (at%)	Sn (at%)	S (at%)
Au MTs	58.8	10.2	25.1	5.6	0.3	—
Au@MUA 11 MTs	60.1	11.6	19.0	2.8	0.2	6.3

corresponds to sulfide-like (S^{2-}) species that are chemisorbed onto the metallic gold surface, indicating strong interaction between sulfur and gold atoms. The second doublet, centered at S $2p_{3/2}$ = 163.3 eV and S $2p_{1/2}$ = 164.5 eV, is attributed to unbound or weakly bound organic sulfur species, such as thiol (R-SH) or disulfide (R-S-S-R) groups that remain after incomplete chemisorption or partial surface coverage.[41]

Furthermore, the survey spectra reveal C 1 s and O 1 s peaks that become significantly more intense after MUA11 modification compared to the pristine Au MTs. This enhancement is consistent with the organic nature of MUA11, which contains carbon- and oxygen-rich carboxylic acid and alkyl groups.

The Au 4f spectra are presented in Fig. 3c and d. Au $4f_{7/2}$ and Au $4f_{5/2}$ in the binding energy range of 84–88 eV. In the spectrum of pristine Au MTs (Fig. 3c), these gold peaks are intense and well-defined, reflecting a clean metallic surface. After surface modification with MUA11 (Fig. 3d), the positions of the Au $4f_{7/2}$ and Au $4f_{5/2}$ peaks remain at approximately 84.0 eV and 87.7 eV, respectively, indicating that the gold retains its metallic state upon functionalization.

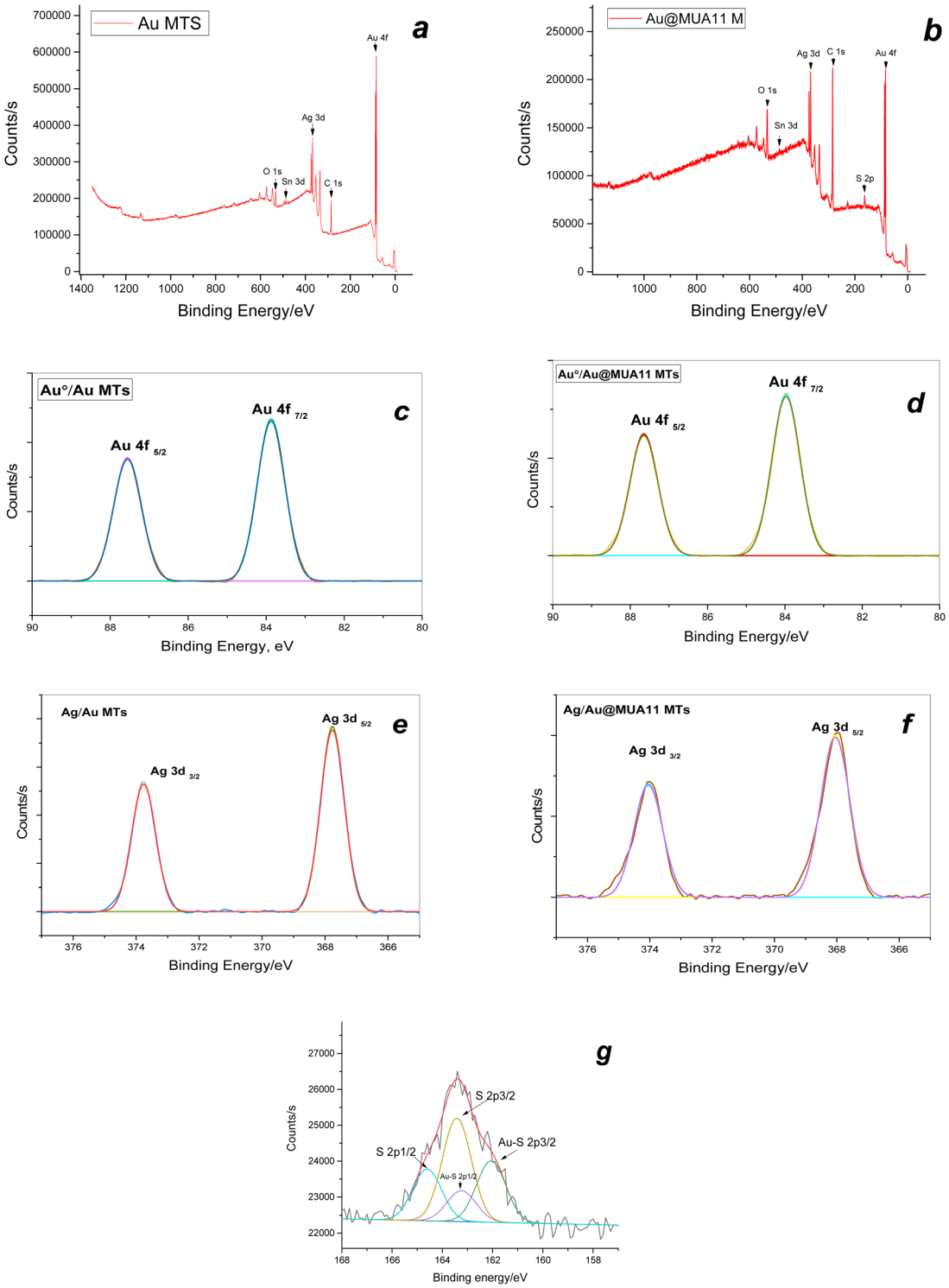

Fig. 3 Survey XPS spectra of Au MTs (a) and Au@MUA11 MTs (b); Au 4f peaks of Au MTs (c) and Au@MUA11 MTs (d); Ag 3d peaks of Au MTs (e) and Au@MUA11 MTs (f); S 2p peaks of Au@MUA11 MTs (g).

In addition to Au, distinct peaks characteristic of Ag is observed at 368 eV and 374 eV, corresponding to Ag $3d_{5/2}$ and Ag $3d_{3/2}$ respectively (Fig. 3e and f). The positions of these Ag 3d peaks are consistent with metallic silver, confirming the coexistence of both Au and Ag components within the sample before and after modification with MUA11.[42] The elemental composition derived from the XPS survey spectra is summarized in Table 2.

The Table 3 summarizes the structured parameters of the PET template and the synthesized gold microtubes. The pristine

Table 3 Summary of gas permeability parameters for Au MTs

Sample	Pore diameter (μm)	Channel length (μm)	Wall thickness (μm)	Mass of synthesized microtubes per membrane (mg cm^{-2})
PET membrane	1.5 ± 0.23	≤ 12.0	—	—
PET membrane with gold microtubes	1.4 ± 0.21	≤ 12.0	0.1 ± 0.015	0.625 ± 0.09

PET membranes possess pores with an average diameter of 1.5 ± 0.23 μm and a channel length of up to 12 μm. After electrochemical deposition of gold, the resulting microtubes exhibit slightly reduced pore diameters (1.4 ± 0.21 μm), which indicates partial wall formation within the template channels. The wall thickness of the gold microtubes does not exceed 0.1 ± 0.015 μm, while the overall mass of microtubes synthesized per membrane ranges from 0.625 mg cm^{-2} ± 0.09.

3.2 UV-vis adsorption

The UV–Vis absorption spectra of Au and Au@MUA11 MTs are shown in Fig. 4a. The initial LSPR analysis was carried out using a UV–Vis spectrometer. For Au MTs and Au@MUA11 MTs, no narrow or well-resolved plasmon resonance peaks were observed. Instead, the UV-vis spectra (Fig. 4a) exhibit a broad absorption band centered in the 440–470 nm range, arising from collective plasmon oscillations in the nanostructured microtubes.[43]

Notably, the Au@MUA11 MTs demonstrate lower absorption intensity compared to the pristine Au MTs, indicating a reduced plasmonic response after surface modification. This effect may be associated with changes in the local dielectric environment and interparticle interactions induced by the MUA11 layer.

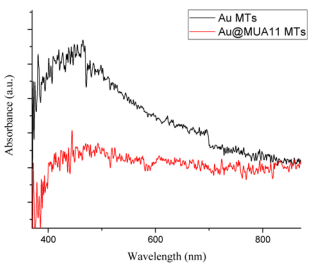

Fig. 4 UV-Vis absorbtion spectra of Au and Au@MUA11 MTs.

3.3 SERS analysis

The SERS spectra of the dye solutions were analyzed before and after modification of the gold microtubes. As shown in Fig. 5, the spectra of the Au (a) and Au@MUA11 (b) samples after thorough washing exhibit almost no additional Raman bands, with signals remaining at the noise level. Additional experiments performed under insufficient washing conditions revealed the presence of weak S–H vibrational bands in the 2500–3000 cm^{-1} region, indicating residual unbound MUA11 molecules. These features disappear after repeated washing with isopropanol, confirming effective removal of non-chemisorbed species. The corresponding data is provided in the SI (Fig. S1). At the same time, XPS analysis (Section 3.2) demonstrated that the covalently bound MUA11 molecules remain anchored to the gold surface, supporting the successful surface modification of Au MTs. The difference between Raman and XPS results is attributed to their different probing depths. SERS detects only molecules in electromagnetic hotspots, while XPS detects all surface species, including weakly bound molecules outside the SERS-active regions.

Thiol-terminated ligands have been shown to influence the physicochemical properties of gold nanostructures. Among them, MUA11 has been extensively employed to stabilize gold nanoclusters and nanoparticles due to its strong Au–S bonding and carboxyl terminal groups, which enable further chemical functionalization.[22,28,30] Such modification improves the stability and dispersibility of gold nanostructures and provides anchoring sites for biomolecules, making them highly attractive for SERS applications. As complementary examples, other thiol ligands such as mercaptosuccinic acid (MSA) have also been investigated, showing effects on electron transfer and surface reactivity of gold.[44]

Next, the effect of recording the spectrum from different micro-zones was investigated, as shown in the (Fig. 6). The micrograph illustrates the distribution of Au microtubes and

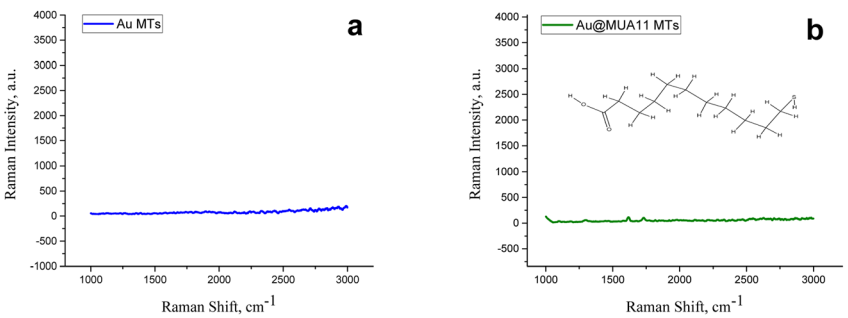

Fig. 5 Raman spectra recorded at an excitation wavelength of 532 nm: (a) Au sample, (b) AuMUA11 after thorough washing.

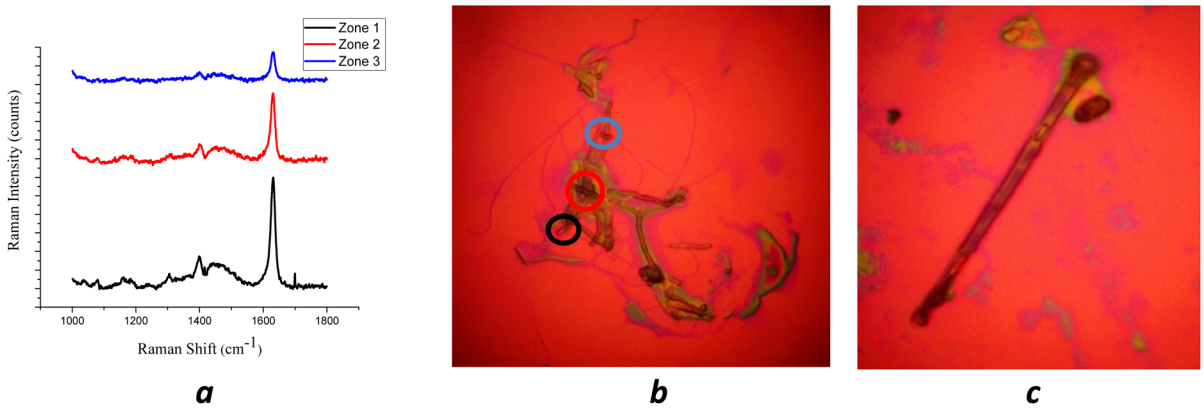

Fig. 6 (a) Methyl blue at a concentration of 10^{-5} M in three different locations on the Au MTs; (b) optical images obtained from SERS of three zones; (c) SERS microscope image of Au MTs at 50× magnification.

their interaction with methylene blue molecules at a concentration of 1×10^{-5} M. Spectra collected from different regions of the substrate revealed three characteristic zones. (Zone 1) A pronounced SERS signal was observed, which can be attributed to the efficient adsorption of dye molecules onto well-dispersed Au microtubes. (Zone 2) In this region, the spectral intensity was noticeably weaker. This reduction can be explained either by excessive aggregation of microtubes, which screens the electromagnetic field and reduces the number of accessible active sites, or by uneven dye adsorption. (Zone 3) Here in, the signal was suppressed due to insufficient adsorption of methylene blue molecules. Such behavior occurs when the substrate loses dispersibility, making the Au surface less accessible for analyte molecules. Overall, not only the chemical interaction between methylene blue and Au but also the morphological characteristics of the substrates play a crucial role. Proper dispersibility and uniform distribution of Au microtubes provide a higher number of active sites, thereby improving both the reproducibility and intensity of the SERS response.

Fig. 7 shows the SERS spectra of three dye molecules methylene blue (a, b), methyl violet (c, d), and methyl red (e, f) recorded at different concentrations ranging from 10^{-6} M to 10^{-2} M for methylene blue/methyl violet and 10^{-6} M to 10^{-3} M for methyl red using Au (a, c, e) and Au@MUA11 (b, d, f) microtubes as active substrates. The measurements were performed exclusively from zone 1, located at the edges of microtube clusters, where the local electromagnetic field is expected to be strongest due to the formation of interparticle plasmonic junctions ("hot spots"). In all cases, a progressive enhancement of characteristic Raman bands was observed with increasing analyte concentration, demonstrating the reproducibility and sensitivity of both types of substrates. The spectra exhibit well-defined vibrational features corresponding to the molecular structures of the dyes.[45]

Fig. 8 presents the calibration plots of Raman peak area *versus* logarithm of concentration for three model dyes methylene blue, methyl violet, and methyl red measured on Au and Au@MUA11 microtube substrates. The corresponding analytical parameters, including the main vibrational bands (cm^{-1}), enhancement factor (EF), correlation coefficients (R^2), and limits of detection (LOD), are summarized in Table 4. LOD was calculated based on peak areas. A clear linear relationship is observed between the Raman peak area and the logarithm of dye concentration for all systems, confirming the quantitative potential of SERS analysis.

For methylene blue, the characteristic peaks at 1400 cm^{-1} and 1625 cm^{-1} exhibit linearity ($R^2 \approx 0.92$–0.98). The Au@MUA11 substrate provides markedly stronger enhancement than bare Au, especially for the 1400 cm^{-1} band (EF = 0.02×10^4 *vs.* 0.4×10^4).

This observation is quantified by a 20-fold increase in the Enhancement Factor (EF) for the 1400 cm^{-1} peak, which is attributed to the electrostatic attraction between the cationic dye and the anionic carboxyl groups of the MUA11 layer. However, a discrepancy is observed for the 1625 cm^{-1} peak: while its EF increases slightly, its LOD worsens (from 0.99 to 2.3 μM). This highlights the difference between the EF, a physical measure of molecular signal boost, and the LOD, an analytical parameter governed by the signal-to-noise ratio and calibration linearity. The increased intensity at 1400 cm^{-1} upon modification makes it a more robust analytical marker, whereas the 1625 cm^{-1} mode, despite its higher absolute intensity, suffers from reduced correlation ($R^2 = 0.92$).

In order to verify the correctness of the spectral identification, the experimentally observed Raman bands were compared with previously reported SERS data for the corresponding dyes. For methylene blue, the characteristic bands detected at around 1400 cm^{-1} and 1625 cm^{-1} are in good agreement with literature reports, where the band near 1625 cm^{-1} is commonly assigned to ring C–C and C–N stretching vibrations and is used as the main analytical feature. The detection limit achieved for methylene blue falls within the 10^{-5}–10^{-6} M range, which is consistent with literature reports on SERS detection, where limits of 10^{-7}–10^{-6} M have been reported depending on the substrate and experimental conditions.[46]

For methyl violet, the dominant peaks at 1370 cm^{-1} and 1620 cm^{-1} demonstrate a similar trend. The EF increases by nearly one order of magnitude on Au@MUA11 (~0.2×10^4 *vs.* 0.02×10^4 on Au), accompanied by a strong linear correlation ($R^2 \approx 0.97$) and a reduction of LOD from approximately 15.8–

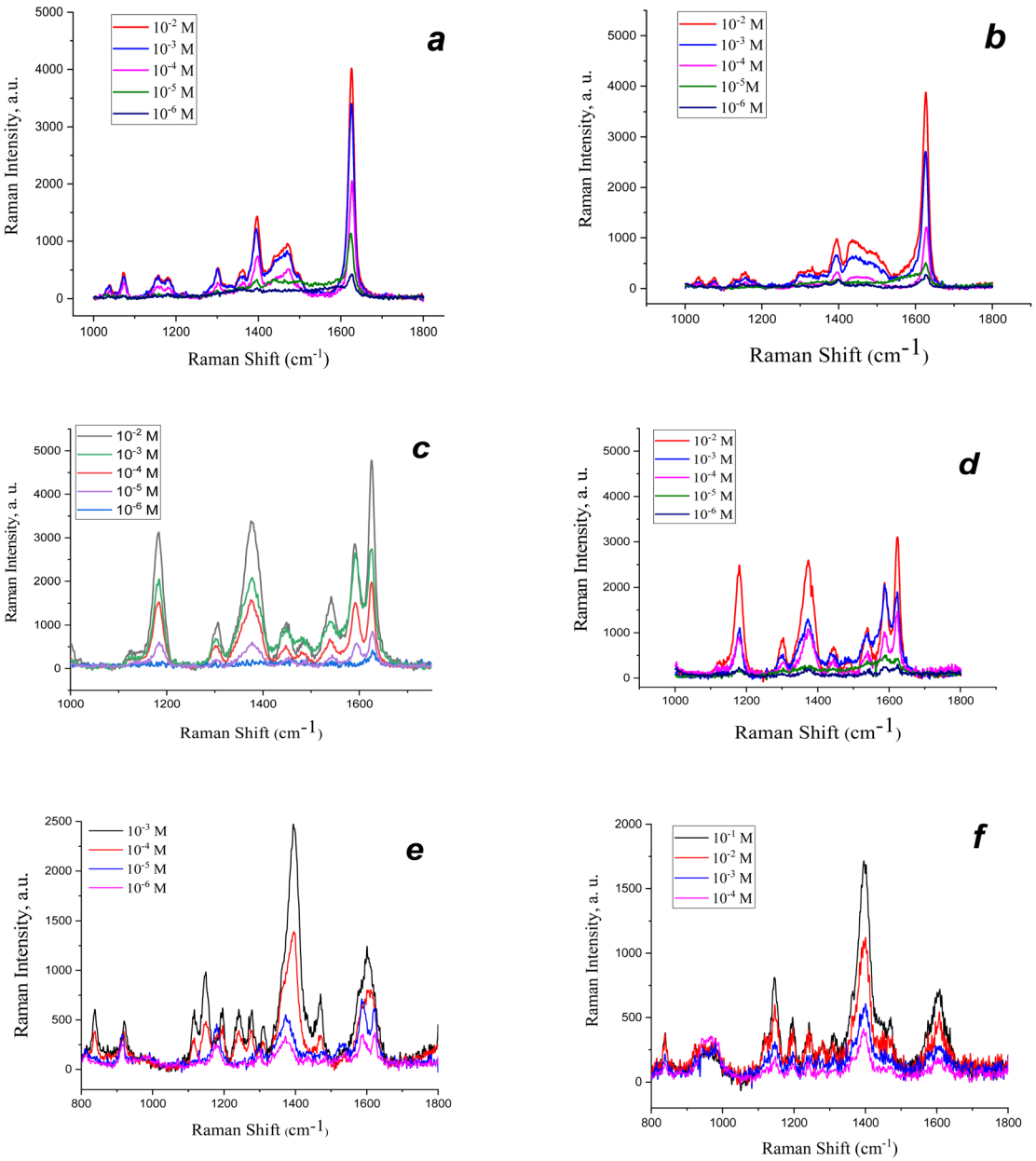

Fig. 7 SERS spectra. (a) Methylene Blue on Au substrates at concentrations ranging from 10^{-2} to 10^{-6} M; (b) Methylene Blue on Au@MUA11 substrates at concentrations ranging from 10^{-2} to10^{-6} M; (c) Methyl Violet on Au substrates at concentrations ranging from 10^{-2} to 10^{-6} M; (d) Methyl Violet on Au@MUA11 substrates at concentrations ranging from 10^{-2} to 10^{-6} M; (e) Methyl Red on Au substrates at concentrations ranging from 10^{-3} to 10^{-6} M; (f) Methyl Red on Au@MUA11 substrates at concentrations ranging from 10^{-3} to 10^{-6} M.

1.98 μM. This pronounced enhancement is attributed electromagnetic coupling and electrostatic attraction between the positively charged dye and the negatively charged carboxyl-functionalized surface, leading to denser molecular adsorption and stronger SERS response. For methyl violet, the observed characteristic peaks at approximately 1370 cm^{-1} and 1620 cm^{-1} are consistent with reported SERS spectra, which typically show prominent bands in the 1370–1380 cm^{-1} and 1580–1620 cm^{-1} regions corresponding to ring-related vibrational modes.[47] According to the literature data, the obtained LOD value corresponds to the average and stable direction characteristic of SERS detection of cationic dyes on gold substrates.[48]

Methyl red is an azo dye characterized by conjugated π-electron system containing an –N=N– linkage between aromatic rings, which governs it vibrational behavior. The dominant Raman band observed at 1390 cm^{-1} is assigned to the azo (–N=N–) stretching vibration, typically reported in the 1380–1400 cm^{-1} region for azo dyes. The band near 1600 cm^{-1} corresponds to C=C and C=N stretching vibrations of the quinonoid ring structure, associated with π-electron delocalization and protonation effects.

These assignments are consistent with previously reported Raman and SERS studies of methyl red and related azo dyes, where bands in the 1387–1396 cm^{-1} and 1590–1620 cm^{-1}

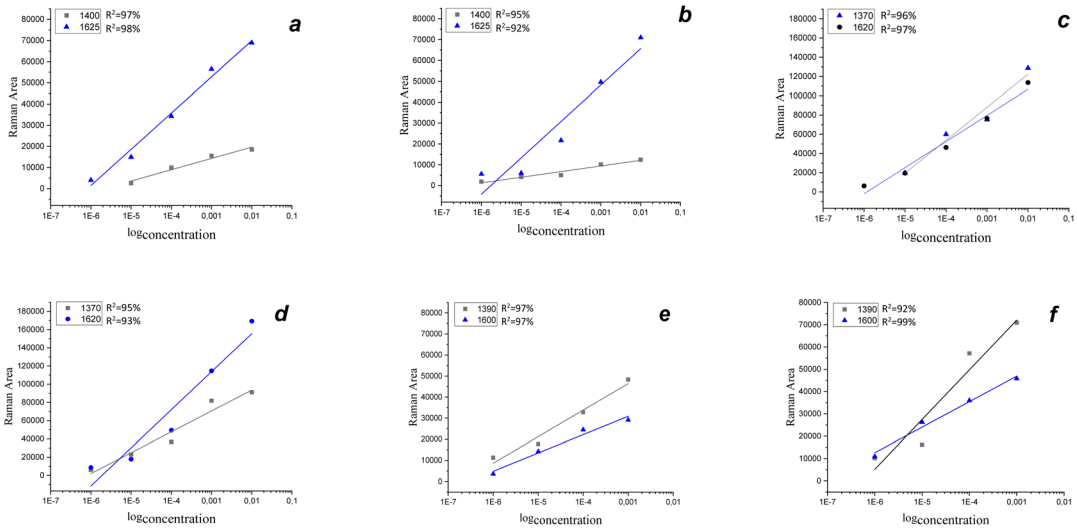

Fig. 8 (a) Au substrates calibrated at 1400 and 1625 cm^{-1} using methylene blue; (b) Au@MUA11 substrates calibrated at 1400 and 1625 cm^{-1} using methylene blue; (c) Au substrates calibrated at 1370 and 1625 cm^{-1} using methyl violet; (d) Au@MUA11 substrates calibrated at 1370 and 1625 cm^{-1} using methyl violet; (e) Au substrates calibrated at 1390 and 1600 cm^{-1} using methyl red; (f) Au@MUA11 substrates calibrated at 1390 and 1600 cm^{-1} using methyl red.

Table 4 Analytical parameters from SERS measurements

Dyes	Substrate	Peaks, (cm^{-1})	EF ($\times 10^4$)	R^2, %	LOD, μM
Methyl blue	Au	1400	0.02	97	15.4
		1625	0.3	98	0.99
	Au@MUA	1400	0.4	95	1.9
		1625	0.4	92	2.3
Methyl violet	Au	1370	0.02	96	15.8
		1620	0.01	97	11.9
	Au@MUA	1370	0.2	95	1.98
		1620	0.2	93	1.97
Methyl red	Au	1390	0.6	97	1.89
		1600	0.6	97	1.8
	Au@MUA	1390	0.6	92	3.13
		1600	0.2	99	1.3

regions are commonly attributed to azo stretching and aromatic ring vibrations.[49] In particular, the spectral features of methyl red are known to depend on protonation state and adsorption environment, leading to the coexistence of azo and quinonoid forms and corresponding shifts in vibrational modes.[50] Furthermore, similar SERS responses and detection limits on the order of 10^{-6} M have been reported for methyl red using plasmonic substrates such as silver/gold bimetallic nanoframes.[43]

The EF values for methyl red are within $(0.6) \times 10^4$ for Au and $(0.2–0.6)\times 10^4$ for Au@MUA11, with corresponding LOD values of 1.8 μM and 1.3–3.3 μM, respectively.

Overall, the results presented in Fig. 8 and Table 4 demonstrate a clear selectivity trend: the Au@MUA11 substrates are significantly more effective for cationic dyes, providing up to 10-20-folder (methyl violet) higher enhancement factors and lower detection limits compared with bare gold. These findings emphasize the importance of surface charge engineering and molecular electrostatics in designing SERS-active substrates optimized for specific analyte types.

Also, it should be noted that the enhancement factors obtained in this work (10^3–10^4) are lower than those reported for advanced three-dimensional SERS substrates, where values in the range of 10^6–10^8 can be achieved.[45] This difference is mainly attributed to the simpler structural design of the proposed microtube-based substrate, which does not rely on complex hierarchical nanostructures. Nevertheless, the developed system offers a balanced combination of sufficient sensitivity, good reproducibility, and straightforward fabrication.

A detailed comparison of the SERS performance for Au and Au@MUA11 substrates reveals a varies with concentration behavior of surface functionalization effects. At higher analyte concentrations, the non-modified Au substrate often exhibits comparable or even higher signal intensity. This behavior can be attributed to the formation of multilayer adsorption and partial aggregation of dye molecules, in this case, the effect of interaction between the microtube and the dye is not dominate.

In contrast, at low concentrations (10^{-6} M), the effect of surface functionalization becomes more pronounced, as clearly demonstrated in Fig. 9. For methyl violet (Fig. 9a), characteristic Raman bands at 1184, 1375, and 1590 cm^{-1} are more clearly resolved and exhibit higher intensity on the Au@MUA11 substrate, indicating improved adsorption and more efficient hotspot utilization.

A similar trend is observed for methylene blue (Fig. 9b), where the characteristic band at ~1400 cm^{-1} is significantly more pronounced on Au@MUA11 compared to bare Au, confirming enhanced interaction between the cationic dye molecules and the negatively charged surface.

In contrast, methyl red (Fig. 9c), the behavior differs. The signal obtained on bare Au shows higher intensity and better-defined spectral into two components (~1591 and

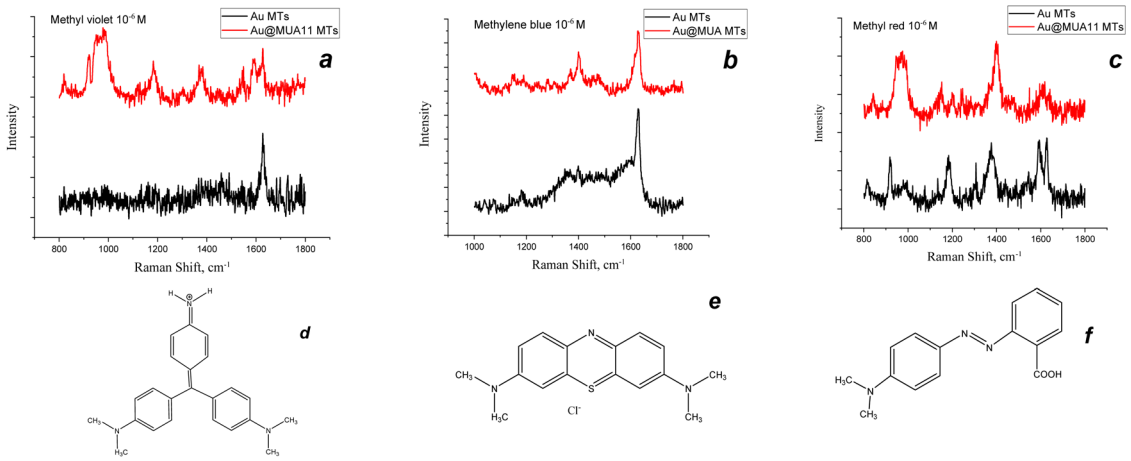

Fig. 9 (a) SERS spectra of Methyl Violet (10^{-6} M) on Au and Au@MUA11 substrates; (b) SERS spectra of Methylene blue (10^{-6} M) on Au and Au@MUA11 substrates; (c) SERS spectra of Methyl Red (10^{-6} M) on Au and Au@MUA11 substrates; chemical structure formulas of the dyes: methyl violet (d), methyl blue (e), and methyl red (f).

~1630 cm^{-1}), which is more clearly observed on the unmodified substrate. This indicates that for anionic dyes, the negatively charged surface of the modified microtube does not promote sorption due to the repulsion of charges. These observations are consistent with the quantitative data presented in Fig. 8 and Table 4, where significant improvements. In EF and LOD are observed for cationic dyes (methylene blue and methyl violet) on Au@MUA11, while only minor or inconsistent changes are detected for methyl red.

Overall, the results demonstrate that MUA11 functionalization enhances SERS performance of cationic dyes. The modification is most effective in the trace concentration regime, where electrostatic interactions promote adsorption, leading to improved spectral quality.[51,52]

4 Conclusions

In summary, the synthesized gold microtube-based substrates modified with 11-mercaptoundecanoic acid (MUA11) demonstrated high structural uniformity, strong plasmonic resonance near 440–470 nm. The XPS analysis confirmed successful organic functionalization, while SERS measurements with methylene blue, methyl violet and methyl red revealed stable and reproducible enhancement across concentrations from 10^{-1} to 10^{-6} M. Findings highlight the strong influence of molecular charge on SERS efficiency and demonstrate that tailored surface functionalization can be used to tune substrate analyte interactions. Thus, Au@MUA11 microtubes show excellent potential for the selective detection of cationic species, offering both high sensitivity and chemical specificity.

Author contributions

Conceptualization, I. V. K. and A. B. K.; methodology, I. V. K.; validation, A. B. K. and I. V. K.; investigation, A. B. K. and I. V. K.; writing-original draft preparation, A. B. K.; writing-review and editing, I. V. K.; supervision, I. V. K.; project administration, I. V. K.; funding acquisition, I. V. K. All authors have read and agreed to the published version of the manuscript.

Conflicts of interest

The authors declare no competing interests.

Data availability

The supporting data have been provided as part of the supplementary information (SI). Supplementary information: corresponding data files for SEM, SERS, UV-vis, XRD and XPS analyses. Also Fig. S1 presented Raman spectra of AuMUA11 after insuffient washing. See DOI: https://doi.org/10.1039/d6ra01224h.

Acknowledgements

This research was funded by the Ministry of Science and Higher Education of the Republic of Kazakhstan (AP23486127, BR28713053). In preparing this manuscript, the authors utilized ChatGPT-5 to enhance the English grammar and style for improved clarity and readability. The original draft and subsequent revisions were written by the authors themselves. Following the use of these tools, the authors thoroughly reviewed and edited the output and assume full responsibility for the final content of this publication.

References

1 I. V. Korolkov, A. Shumskaya, A. L. Kozlovskiy, M. E. Kaliyekperov, L. I. Lissovskaya and M. V. Zdorovets, *J. Alloys Compd.*, 2022, **901**, 163661.
2 A. Shumskaya, I. Korolkov, A. Rogachev, Z. Ignatovich, A. Kozlovskiy, M. Zdorovets, M. Anisovich, M. Bashouti, A. Shalabny, R. Busool, S. Khubezhov, D. Yakimchuk, V. Bundyukova, L. V. Panina and E. Kaniukov, *Colloids Surf., A*, 2021, **626**, 127077.

3 L. Litti and M. Meneghetti, *Phys. Chem. Chem. Phys.*, 2019, **21**, 15515–15522.
4 E. C. Le Ru, E. Blackie, M. Meyer and P. G. Etchegoint, *J. Phys. Chem. C*, 2007, **111**, 13794–13803.
5 T. Y. Jeon, D. J. Kim, S. G. Park, S. H. Kim and D. H. Kim, *Nano Convergence*, 2016, **3**, 18.
6 B. Sharma, M. Fernanda Cardinal, S. L. Kleinman, N. G. Greeneltch, R. R. Frontiera, M. G. Blaber, G. C. Schatz and R. P. Van Duyne, *MRS Bull.*, 2013, **38**, 615–624.
7 W. R. Chang, C. Hsiao, Y. F. Chen, C. F. J. Kuo and C. W. Chiu, *ACS Omega*, 2022, **7**, 41815–41826.
8 H. Zhou, D. Yang, N. P. Ivleva, N. E. Mircescu, R. Niessner and C. Haisch, *Anal. Chem.*, 2014, **86**, 1525–1533.
9 S. Wen, Y. Su, R. Wu, S. Zhou, Q. Min, G. C. Fan, L. P. Jiang, R. Bin Song and J. J. Zhu, *Biosens. Bioelectron.*, 2018, **117**, 260–266.
10 V. S. Vendamani, S. V. S. Nageswara Rao, S. Venugopal Rao, D. Kanjilal and A. P. Pathak, *J. Appl. Phys.*, 2018, **123**, 014301.
11 S. Cheng, Z. Tu, S. Zheng, A. Khan, P. Yang, H. Shen and B. Gu, *Int. J. Nanomedicine*, 2024, **19**, 389–401.
12 F. K. Alsammarraie and M. Lin, *J. Agric. Food Chem.*, 2017, **65**, 666–674.
13 T. Wang, S. Wang, Z. Cheng, J. Wei, L. Yang, Z. Zhong, H. Hu, Y. Wang, B. Zhou and P. Li, *Chem. Eng. J.*, 2021, 130323.
14 X. Zhou, S. Chen, Y. Pan, Y. Wang, N. Xu, Y. Xue, X. Wei and Y. Lu, *Biosensors*, 2023, **13**, 766.
15 W. Zhai, M. Cao, Z. Xiao, D. Li and M. Wang, *Foods*, 2022, **11**, 3597.
16 H. Zhang, Y. Kou, J. Li, L. Chen, Z. Mao, X. X. Han, B. Zhao and Y. Ozaki, *Anal. Chem.*, 2019, **91**, 1213–1216.
17 T. T. Nguyen, S. Lau-Truong, F. Mammeri and S. Ammar, *Nanomaterials*, 2020, **10**, 294.
18 B. Sharma, R. R. Frontiera, A. I. Henry, E. Ringe and R. P. Van Duyne, *Mater. Today*, 2012, **15**, 16–25.
19 M. Park, Y. S. Kim, S. Kim and J. Y. Lim, *J. Hazard. Mater.*, 2025, 137197.
20 K. Karn-orachai, Y. Sanguansap, K. Pankleaub, O. Noppha, N. Wiriyakun, P. Kanatharana and R. laocharoensuk, *Appl. Surf. Sci.*, 2020, **529**, 147236.
21 M. Jing, H. Zhang, M. Li, Z. Mao and X. Shi, *Spectrochim. Acta A Mol. Biomol. Spectrosc.*, 2021, **251**, 119652.
22 S. M. Ansar, S. Chakraborty and C. L. Kitchens, *Nanomaterials*, 2018, **8**, 339.
23 V. Dzhagan, N. Mazur, O. Kapush, M. Skoryk, Y. Pirko, A. Yemets, V. Dzhahan, P. Shepeliavyi, M. Valakh and V. Yukhymchuk, *ACS Omega*, 2024, **9**, 4819–4830.
24 P. Q. T. Do, V. T. Huong, N. T. T. Phuong, T. H. Nguyen, H. K. T. Ta, H. Ju, T. B. Phan, V. D. Phung, K. T. L. Trinh and N. H. T. Tran, *RSC Adv.*, 2020, **10**, 30858–30869.
25 H. Wei, Z. Peng, C. Yang, Y. Tian, L. Sun, G. Wang and M. Liu, *Nanomaterials*, 2021, **11**, 2026.
26 K. Shibusawa, T. Hase and K. Tsukada, *AIP Adv.*, 2019, **9**, 065316.
27 C. Huang, H. Li and X. Zhang, *ACS Omega*, 2024, **9**, 37188–37196.
28 L. Meng, J. H. Yin, Y. Yuan and N. Xu, *RSC Adv.*, 2018, **8**, 9327–9333.
29 J. Xie, L. Li, I. M. Khan, Z. Wang and X. Ma, *Spectrochim. Acta A Mol. Biomol. Spectrosc.*, 2020, **231**, 118104.
30 F. C. Marques, G. P. Oliveira, R. A. R. Teixeira, R. M. S. Justo, T. B. V. Neves and G. F. S. Andrade, *Vib. Spectrosc.*, 2018, **98**, 139–144.
31 F. K. Alsammarraie, M. Lin, A. Mustapha, H. Lin, X. Chen, Y. Chen, H. Wang and M. Huang, *Food Chem.*, 2018, **259**, 219–225.
32 H. Lachheb, E. Puzenat, A. Houas, M. Ksibi, E. Elaloui, C. Guillard and J.-M. Herrmann, *Photocatalytic Degradation of Various Types of Dyes (Alizarin S, Crocein Orange G, Methyl Red, Congo Red, Methylene Blue) in Water by UV-Irradiated Titania*, 2002, vol. 39.
33 O. Olea-Mejía, M. Fernández-Mondragón, G. Rodríguez-De La Concha and M. Camacho-López, *Appl. Surf. Sci.*, 2015, **348**, 66–70.
34 Y.-L. Liu, J. Zhu, G.-J. Weng, J.-J. Li and J.-W. Zhao, *Microchim. Acta*, 2020, **187**, 612.
35 A. A. Mashentseva and M. V. Zdorovets, *Petroleum Chemistry*, 2019, **59**, 552–557.
36 F. Muench, *ChemElectroChem*, 2021, **8**, 2993–3012.
37 A. Mashentseva, D. Borgekov, M. Zdorovets and A. Russakova, in *Acta Physica Polonica A*, Polska Akademia Nauk, 2014, vol. 125, pp. 1263–1266.
38 P. Shao, G. Ji and P. Chen, *J. Memb. Sci.*, 2005, **255**, 1–11.
39 M. E. Hamza, M. A. Othman and M. A. Swillam, *Plasmonic Biosensors: Review, Biology*, 2022, **11**, 621.
40 Z. Huang, J. Peng, L. Xu and P. Liu, *Nanomaterials*, 2024, **14**, 1417.
41 B. Paramanik and A. Patra, *J. Mater. Chem. C Mater.*, 2014, **2**, 3005–3012.
42 J. Stettner, P. Frank, T. Griesser, G. Trimmel, R. Schennach, E. Gilli and A. Winkler, *Langmuir*, 2009, **25**, 1427–1433.
43 X. H. Vu, N. D. Dien, T. T. Ha Pham, N. Van Truong, N. X. Ca and V. Van Thu, *RSC Adv.*, 2021, **11**, 14596–14606.
44 L. Sun, D. Zhao, M. Ding, H. Zhao, Z. Zhang, B. Li and D. Shen, *J. Mater. Sci. Technol.*, 2013, **29**, 613–618.
45 J. Wang, C. Qiu, X. Mu, H. Pang, X. Chen and D. Liu, *Talanta*, 2020, **210**, 120631.
46 X. H. Vu, N. D. Dien, T. T. Ha Pham, T. T. Trang, N. X. Ca, P. T. Tho, N. D. Vinh and P. Van Do, *RSC Adv.*, 2020, **10**, 38974–38988.
47 M. A. El-Aal, T. Seto and A. Matsuki, *Appl. Phys. A:Solids Surf.*, 2020, **126**, 572.
48 J. L. Zamora-Navarro, D. González-Zárate, M. A. Díaz-Solís, M. G. Soriano-Rosales, Y. B. Okolodkov and L. Zamora-Peredo, *Mater. Proc.*, 2022, **9**, 27.
49 R. Giustetto, A. Idone and E. Diana, *J. Raman Spectrosc.*, 2017, **48**, 507–517.
50 S. Lee, J. H. Wong and S. J. Liu, *Appl. Spectrosc.*, 2011, **65**, 996–1003.
51 E. D. B. Santos, N. V. Madalossi, F. A. Sigoli and I. O. Mazali, *New J. Chem.*, 2015, **39**, 2839–2846.
52 X. H. Vu, N. D. Dien, T. T. Ha Pham, N. Van Truong, N. X. Ca and V. Van Thu, *RSC Adv.*, 2021, **11**, 14596–14606.